


ORIGINAL RESEARCH

On the input impedance of probe-fed electromagnetic bandgap antennas based on lattice modes

Silvio Ceccuzzi^{1,2}  | Paolo Baccarelli^{1,3} | Cristina Ponti^{1,3} | Ludovica Tognolatti¹ | Giuseppe Schettini^{1,3}

¹Department of Industrial, Electronic, and Mechanical Engineering, 'Roma Tre' University, Rome, Italy

²Department of Fusion and Nuclear Safety, ENEA, Frascati, Italy

³CNIT, 'Roma Tre' University, Rome, Italy

Correspondence

Silvio Ceccuzzi, Department of Fusion and Nuclear Safety, ENEA, Frascati, Italy.
Email: silvio.ceccuzzi@enea.it

Funding information

Italian Ministry for Education, University, and Research, Grant/Award Number: 20177C3WRM_003

Abstract

The impedance of a coaxial probe, feeding an Electromagnetic Bandgap (EBG) structure conceived for radiation shaping, is studied from the theoretical and numerical viewpoints. The EBG medium is a square arrangement of dielectric cylinders placed in a parallel-plate waveguide, where a suitable lattice mode is excited. A semi-analytical model is developed and used to derive an approximate, closed-form expression of the probe resistance. The model is based on a modal expansion in Floquet harmonics, on which a current distribution is projected according to the Lorentz reciprocity theorem to derive the amplitude of lattice modes propagating right above the bandgap along lattice axes. The dependence of probe impedance on lattice parameters is then investigated with the numerical simulations of a finite-element method, which is also used to validate the developed model. A broad set of parametric analyses is presented, showing that the reactive part weakly depends on probe position, cylinder radius and permittivity, while the heights of probe and parallel-plate waveguide play a major role in determining the resonance condition. As to the probe resistance, it decreases with cylinder radius and permittivity and decreases with probe and waveguide heights. The derived analytical formula correctly reproduces such functional dependences and its calculation is immediate, revealing its usefulness in antenna design. Matching issues are heuristically and experimentally approached by examples, demonstrating that the proposed work can be effectively employed to improve the electrical performance of EBG antennas with an embedded source.

1 | INTRODUCTION

Electromagnetic Bandgap materials (EBGs) are periodic structures where wave propagation is not allowed within some frequency bands. Such feature has been profitably exploited in the last decades to improve the performance of microwave antennas and components, such as waveguides, oscillators, shields and filters [1, 2]. Recent developments in additive manufacturing techniques have further boosted the research in EBG materials, allowing fast prototyping and cheap fabrication of complex geometries [3–5]. Moreover, all-dielectric composite structures are very attractive for higher frequency (i.e. millimetre-wave and THz) applications [6, 7].

In the field of EBG antennas, Enoch et al. proposed a radiation mechanism working with the electromagnetic

configurations allowed by the periodic structure, usually called Bloch waves or Floquet modes or lattice modes [8]. Further works followed, assessing different periodic arrangements [9], comparing this approach to the more widely known Fabry–Perot antennas [10], exploiting degenerate dielectric modes [11], synthesising a Dirac cone dispersion to attain zero-refractive-index metamaterials [12] and designing dual-feed antennas [13]. In particular, a deeper physical insight was achieved by adopting a modal perspective through the powerful tools typical of photonic crystals instead of interpreting the lattice behaviour as a homogeneous epsilon-near-zero metamaterial [14]. In the latter paper, a compact antenna was presented, where the EBG was placed in a parallel-plate waveguide fed by a coaxial probe and an external circuit was used to achieve acceptable matching.

This is an open access article under the terms of the Creative Commons Attribution License, which permits use, distribution and reproduction in any medium, provided the original work is properly cited.

© 2022 The Authors. *IET Microwaves, Antennas & Propagation* published by John Wiley & Sons Ltd on behalf of The Institution of Engineering and Technology.

Rather than exploiting the evanescent waves of the lattice bandgap [15], Enoch's radiation mechanism relies on the propagating waves of the lattice bands, especially on the modes right above the bandgap. It follows that the radiation of electromagnetic energy is the result of a twofold process as sketched in Figure 1: (i) the conversion of a feeding wave into some lattice mode and (ii) the conversion of the latter into directive free-space radiation. The former is a coupling problem between the set of modes of a coaxial cable and those of a square lattice. In practical applications, the coaxial feeder only supports the propagation of the fundamental TEM mode that has to be matched to the Floquet mode of interest in the lattice to maximise the power transfer. The second step of the process consists in the propagation of the Floquet mode inside the finite-size lattice and its leakage outside in the form of directive radiation. So far most efforts have been devoted to the second step, whereas this paper addresses the first part of the process, focussing on a probe-fed parallel-plate waveguide loaded with an EBG structure made of dielectric cylinders.

The lattice mode in charge of directive radiation propagates in the plane perpendicular to the axis of the cylinders, with the electric field parallel to and constant along such axis, that is, translational invariance is assumed along cylinders. These are the working conditions that have been assumed since the pioneering works on the topic [16]. To reproduce a similar situation in realistic antennas, either very long cylinders compared to the wavelength [17] or electrically short cylinders sandwiched between two parallel metal plates [14] have been adopted. In both cases, the lattice mode travels over the periodicity plane of the lattice up to its truncation, which constitutes the open boundary where the electromagnetic energy leaks out of the array of cylinders, assuming little or no reflection.

The excitation by finite sources of microwave antennas and devices based on infinite periodic structures and the study of the relevant input impedance is a challenging topic, which has been reported in a few papers in the scientific literature. Semi-analytical approaches based on asymptotic boundary conditions in the large wavelength regime have been used to derive the input impedance of a probe protruding from a coaxial line into an infinite corrugated rectangular metaguides in ref. [18]. An indirect approach, which uses both custom Method of Moments (MoM) procedures and commercial electromagnetic software, has been applied in ref. [19] for determining the equivalent admittance of a slot in a periodic waveguide.

Rigorous full-wave analysis of the input impedance calculated by means of the Array Scanning Method in conjunction with different types of electric field integral equations to solve the MoM has been developed in refs. [20, 21] for 1-D periodic shielded microstrip and 2-D periodic leaky-wave structures respectively.

In this paper, a semi-analytical parallel-plate waveguide approach, which allows for the approximate closed-form expression of the probe resistance in EBG antennas, is adopted. As far as the impedance of a coaxial probe in the parallel-plate waveguide is concerned, Harrington provided a simple formula [22] in 1961. Microstrip antennas boosted significant advancements in this field: accurate closed-form expressions were derived for rectangular patches in ref. [23], numerical techniques for patches of arbitrary shape were developed in ref. [24] and Harrington's formula was generalised to complex impedances of rectangular and circular patches in ref. [25]. An effective approach is the modal-expansion cavity model [26] that analytically solved the coupling problem between the probe of a coaxial feeder and the set of modes of a microstrip antenna modelled as a cavity. A similar approach can be pursued in the geometry dealt in this paper, where, in place of a homogeneous medium, a square lattice of dielectric cylinders is present between the ground plane and the top metal plate so that lattice modes take the place of cavity modes. Parallel-plate waveguides loaded with cylindrical structures were deeply studied with reference to multilayer PCBs and packages [27, 28], where nevertheless modelling efforts focussed on vias, that is, non-periodic, metal cylinders. As to the case of dielectric cylinders, it has been mostly studied with reference to scattering problems [29] that do not deal with impedance issues and coaxial probes.

To the best of authors' knowledge, this paper approaches a probe-fed parallel-plate waveguide, loaded with a lattice of dielectric cylinders with period comparable to the wavelength, for the first time under a theoretical and parametric perspective. Previous documented attempts to address the problem [14] were heuristic and did not explore the parameter space of the probe impedance, but employed an external matching network to achieve a low enough reflection coefficient. Here, an original, modal, semi-analytical model is developed to derive a closed-form expression of the probe resistance that, though unable to predict the exact value of the input resistance of real antennas due to the use of some physical approximations, correctly unveils its functional dependences on the main probe

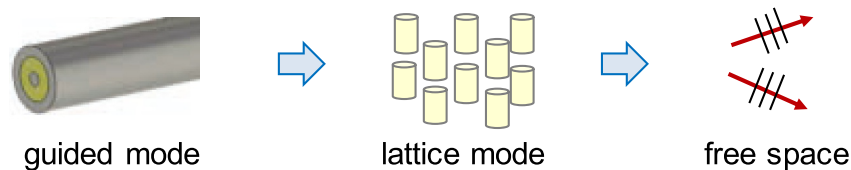


FIGURE 1 Schematic view of the radiation mechanism: the coaxial feeder excites a lattice mode of the electromagnetic bandgap (EBG) structure that achieves directive radiation. The EBG acts as a spatial filter: it takes the electromagnetic energy of the guided mode and radiates it in the free space within narrow angular cones

and lattice parameters. Such dependences along with those of the probe reactance are then parametrically investigated with a finite-element method. The presented study provides fundamental guidelines and directions for the improvement of antenna matching in such class of EBG radiators.

The paper is organised as follows: in Section 2 a theoretical model of the probe impedance is built and a simple, approximate formula of the input resistance is derived. In Section 3, the dependence of the probe impedance with respect to lattice parameters is numerically studied and both semi-analytical and analytical predictions of the input resistance are validated. In Section 4, the problem of matching is briefly addressed by examples. Conclusions are drawn in Section 5.

2 | ANALYTICAL FRAMEWORK

2.1 | Lattice modes

Consider a square lattice of dielectric cylinders in a parallel-plate waveguide, as the one shown in Figure 2. The lattice period is a and the cylinders have height h along z , radius r and relative permittivity ϵ_r . If h does not exceed a few tenths of wavelength, the electromagnetic field is constant along z and the homogeneous wave equation is the same eigenvalue problem as in a two-dimensional lattice when the in-plane propagation of TM^z waves is considered. The electromagnetic field thus consists in a set of lattice modes with components E_z, H_x and H_y , as typical of EBG antennas with embedded sources [14]. A time dependence $e^{j\omega t}$ is assumed.

In the above-mentioned conditions, the electric field of any lattice mode can be expressed as [30]:

$$E_z^\pm(x, y) = \left[\sum_m \sum_n f_{mn} e^{j\left(\frac{2m\pi}{a}x + \frac{2n\pi}{a}y\right)} \right] e^{\mp j(k_x x + k_y y)} \quad (1)$$

where the summations extend from $-\infty$ to ∞ and the \pm signs in E_z denote progressive and regressive waves respectively. The Fourier series in square brackets represent the expansion in Floquet harmonics of a periodic function with period a . The Fourier coefficients f_{mn} are the eigenvectors of the wave equation for a given combination of in-plane propagation vector $\mathbf{k} = k_x \hat{\mathbf{x}} + k_y \hat{\mathbf{y}}$ and frequency band. The latter is the

eigenvalue of such equation and it is usually plotted in the form of a band diagram along the edge of the irreducible Brillouin zone. An example of such plot is depicted in Figure 3a for a square lattice with $a = 10$ mm, $r = 0.35a$ and $\epsilon_r = 11.7$.

The magnetic field components is readily derived from Maxwell equations as

$$\mathbf{H}^\pm(x, y) = -\frac{1}{j\omega\mu_0} \left(\frac{\partial E_z^\pm}{\partial y} \hat{\mathbf{x}} - \frac{\partial E_z^\pm}{\partial x} \hat{\mathbf{y}} \right) \quad (2)$$

where ω is the angular frequency and μ_0 is the vacuum magnetic permeability.

We focus on the modes at the bottom of the air band, which are allowed at 8 GHz in the lattice of Figure 3a. More precisely we restrict the analysis to the mode with $k_x = 0$ and $k_y = \pi/a$, which is used to achieve directive broadside antennas and will be referred to as radiation mode in the following. It is identified more clearly in Figure 3b, where the three-dimensional dispersion diagram of the lattice of Figure 3a is plotted. A mode with $k_x = \pi/a$ and $k_y = 0$ can also propagate at the same frequency, but it has been shown that single modes can be selectively excited in a square lattice [31]. Any lattice mode different from the radiation one will be referred to as spurious or unwanted mode.

2.2 | Input impedance

When a current distribution \mathbf{J} , like the one due to the coaxial probe of Figure 2 is impressed in the parallel-plate waveguide, the lattice modes that are allowed at source frequency may be excited. If the mode with $k_x = 0$ and $k_y = \pi/a$ at the bottom of the air band is only considered, its amplitude can be derived using the Lorentz reciprocity theorem [22]

$$\oint_{\mathcal{S}} (\mathbf{E}_1 \times \mathbf{H}_2 - \mathbf{E}_2 \times \mathbf{H}_1) \cdot \hat{\mathbf{n}} d\mathcal{S} = \iiint_V \mathbf{E}_2 \cdot \mathbf{J} dV \quad (3)$$

with

$$\begin{aligned} \mathbf{E}_1 &= A^+ E_z^+ \hat{\mathbf{z}} + A^- E_z^- \hat{\mathbf{z}} \\ \mathbf{H}_1 &= A^+ \mathbf{H}^+ + A^- \mathbf{H}^- \\ \mathbf{E}_2 &= E_z^- \hat{\mathbf{z}} \\ \mathbf{H}_2 &= \mathbf{H}^- \end{aligned} \quad (4)$$

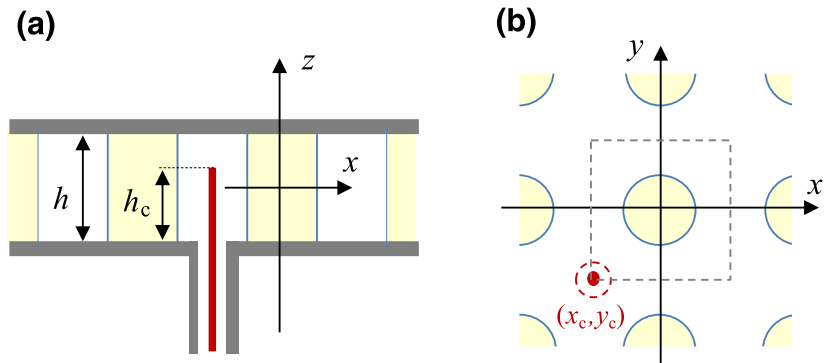


FIGURE 2 Side (a) and top (b) cut views of a probe-fed parallel-plate waveguide, loaded with an electromagnetic bandgap (EBG) structure. The dashed grey square denotes the contour of the unit cell

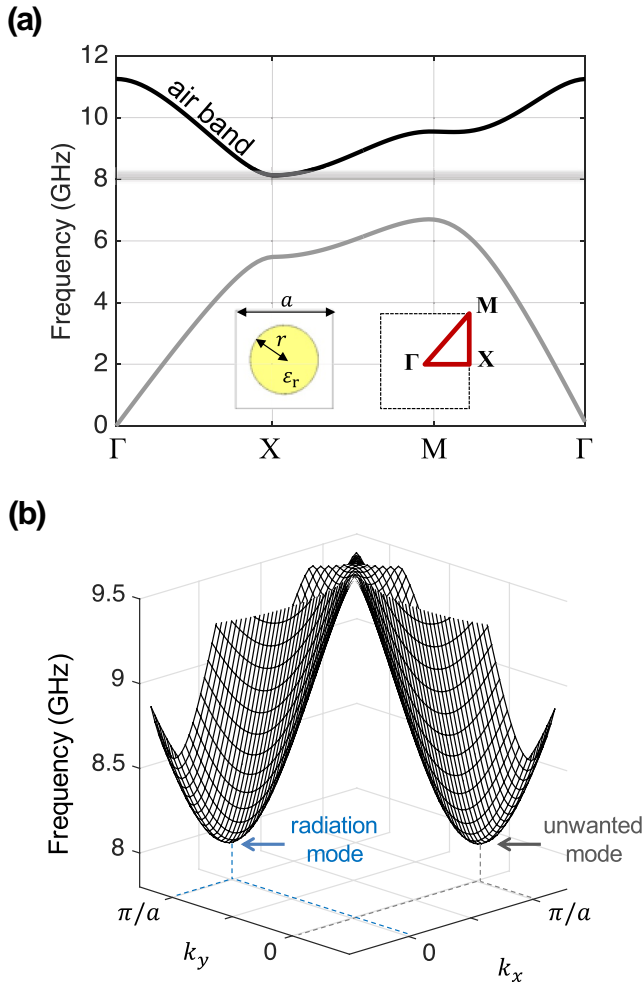


FIGURE 3 Band diagram along the edge of the irreducible Brillouin zone (a) and three-dimensional plot of the air band (b) for a square lattice of Silicon cylinders with $a = 10$ mm, $r = 0.35a$ and $\epsilon_r = 11.7$

The subscript 1 denotes the fields produced by the source $\mathbf{J}_1 = \mathbf{J}$, while the subscript 2 denotes the fields produced by the source $\mathbf{J}_2 = 0$, that is, a *test* source-free solution that is chosen equal to the radiation mode propagating towards $y = -\infty$. With reference to Figure 2, for a thin coaxial probe, the current density can be approximated as

$$\mathbf{J} = I(z)\delta(x - x_c)\delta(y - y_c)\hat{\mathbf{z}} \quad (5)$$

where δ stands for the Dirac delta function and

$$I(z) = \begin{cases} I_0 \cos[k_0(b_c/2 - z)], & \text{if } b_c = b \\ I_0 \sin[k_0(b_c - b/2 - z)], & \text{if } b_c < b \end{cases} \quad (6)$$

with $k_0 = \omega/c$, being c the speed of light in vacuum [32]. By using previous expressions into (3) and taking V as the volume of a unit cell (S is the surface enclosing V), the following expression can be derived for A^+ :

$$A^+ = \frac{E_z^-(x_c, y_c) \int_{-b/2}^{b/2} I(z) dz}{\int_{-b/2}^{b/2} \int_{-a/2}^{a/2} (E_z^+ H_x^- - E_z^- H_x^+) \big|_{y=a/2} dx dz} \quad (7)$$

The denominator of Equation (7) with the use of Equations (1) and (2) becomes

$$-\frac{2\pi b}{\omega\mu_0} \sum_m \sum_n \sum_p \sum_q f_{mn} f_{pq} e^{i\pi(n+q)} \text{sinc}[\pi(m+p)]$$

where $\text{sinc}(x) = \sin(x)/x$. The wave amplitude A^- can be similarly derived choosing the test fields \mathbf{E}_2 and \mathbf{H}_2 equal to the radiation mode propagating towards $y = +\infty$. Due to symmetry, $A^- = A^+$ as in rectangular waveguides [33].

From the electromagnetic field excited by the probe, the input impedance of the feeder at the reference plane $z = -b/2$ is defined as [34].

$$Z_{\text{in}} = R_{\text{in}} + jX_{\text{in}} = \frac{P_r + 2j\omega(W_m - W_e)}{\frac{1}{2}|I(z = -b/2)|^2} \quad (8)$$

where P_r represents the power radiated into the EBG-loaded parallel-plate waveguide, while $W_m - W_e$ is the reactive energy stored in the vicinity of the probe. The latter is due to the excitation of evanescent modes and cannot be expressed in a simple analytical form of practical use, hence it will not be derived in this paper. The dependence on physical parameters would be indeed not so clear and, nowadays, the calculation of X_{in} would be easier with general-purpose software. On the contrary, attention will be paid to R_{in} because a compact approximate expression can be derived, conveying a clear picture of the analytical dependences of the input resistance on lattice parameters.

The radiated power can be calculated as the flux of Poynting vector across the unit-cell volume:

$$\begin{aligned} P_r &= \frac{1}{2} \oint_S \mathbf{E} \times \mathbf{H}^* \cdot \hat{\mathbf{n}} dS \\ &= \frac{|A^+|^2}{2} \int_{-b/2}^{b/2} \int_{-a/2}^{a/2} E_z^+ H_x^{+*} \big|_{y=a/2} dx dz + \\ &\quad - \frac{|A^-|^2}{2} \int_{-b/2}^{b/2} \int_{-a/2}^{a/2} E_z^- H_x^{-*} \big|_{y=-a/2} dx dz \end{aligned} \quad (9)$$

By using Equations (1) and (2), the radiated power becomes

$$\begin{aligned} P_r &= |A^+|^2 \frac{\pi b}{\omega\mu_0} \sum_m \sum_n \sum_p \sum_q f_{mn} f_{pq}^* \\ &\quad \cdot \cos[\pi(n-q)] \text{sinc}[\pi(m-p)] \end{aligned} \quad (10)$$

2.3 | Closed-form expression of R_{in}

A simple approximate formula of the input resistance is now derived to analytically exemplify the functional dependences of R_{in} on lattice parameters. By truncating the summations in Equation (1) to very few terms, the electric field can be written as

$$\begin{aligned} E_z^+ &= \left[1 + b \sin^2\left(\frac{\pi x}{a}\right) \right] \sin\left(\frac{\pi y}{a}\right) e^{-j\frac{2\pi y}{a}} \\ E_z^- &= \left[1 + b \sin^2\left(\frac{\pi x}{a}\right) \right] \sin\left(\frac{\pi y}{a}\right) \end{aligned} \quad (11)$$

with

$$b = \frac{4\kappa_1}{5\kappa_0 - 2\kappa_1 + 5\kappa_2 - (k_0 a / \pi)^2} \quad (12)$$

where

$$\kappa_\ell = \left(\frac{1}{\varepsilon_r} - 1 \right) \frac{r}{\ell a} J_1\left(\frac{2\pi\ell r}{a}\right) + \delta_{\ell 0} \quad (13)$$

The derivation of Equation (11) is reported in the Appendix 1; multiplication factors have been removed because they play no role with reference to the input resistance.

In assembling the real part of Equation (8) by using Equations (10) and (7), a term depending on the current distribution over the probe can be identified. It is

$$\begin{aligned} C_I &= \left| \frac{\int_{-b/2}^{b/2} I(z) dz}{I(z = -b/2)} \right|^2 \\ &= \frac{1}{k_0^2} \cdot \begin{cases} \tan^2(k_0 b_c), & \text{if } b_c = b \\ \tan^2(k_0 b_c / 2), & \text{if } b_c < b \end{cases} \end{aligned} \quad (14)$$

which can be recast into a single formula as

$$C_I = \frac{1}{k_0^2} \tan^2\left(\frac{k_0 b_c}{2 - \delta_{b, b_c}}\right), \quad (15)$$

where $\delta_{m,n}$ denotes the Kronecker delta function, equal to 1 for $m = n$ and 0 for $m \neq n$. With previous definition, the approximate expressions (11) for the electric field, applied to the real part of Equation (8), give

$$R_{in} = C_I \frac{\omega \mu_0 \sin^2\left(\frac{\pi x_c}{a}\right) [2 + b - b \cos\left(\frac{2\pi x_c}{a}\right)]^2}{\pi b (8 + 8b + 3b^2)} \quad (16)$$

The same expression holds true for the degenerate lattice mode with $k_x = \pi/a$ and $k_y = 0$, provided that x_c is replaced with y_c and vice versa. It must be kept in mind that, in Equation (16), the axis origin is taken at the centre of a cylinder.

3 | NUMERICAL RESULTS

3.1 | FEM model and simulation settings

The input impedance of a probe-fed parallel-plate waveguide loaded with the lattice of Figure 3 has been numerically computed with a commercial code based on the finite-element

method (FEM). The real part of Z_{in} has been compared with the results from the semi-analytical model of Section 2.

The geometry of the FEM code is depicted in Figure 4. Metal vias along cylinder rows have been added in the lattice to hamper the unwanted mode with $k_x = \pi/a$ and $k_y = 0$ from propagating at the same frequency of the radiation mode. Such expedient allows the lattice to become monomodal at the bottom of the air band and achieve better radiation performance, without affecting the radiation mode [14]. The material of metal vias has been simulated as perfect electric conductor (PEC). A standard 50-Ω coaxial probe with inner and outer diameters of 1.3 and 4.1 mm, respectively, has been adopted as feeder.

The geometry of a FEM simulation must be finite in extent, hence, in the xy plane, the simulation domain has been cut in the shape of an ellipse, surrounded by PEC. The axes of the ellipse are aligned to the x and y axes, along which there are $(2N_x + 1)$ and $(2N_y + 1)$ cylinders respectively (see Figure 4). To prevent outgoing waves from being reflected at the ellipse metallic border, that is, to emulate an infinite lattice along the x and y directions, an inhomogeneous electrical conductivity of the form

$$\sigma = \frac{1}{\sqrt{1 - \left[\left(\frac{x}{N_x a}\right)^2 + \left(\frac{y}{N_y a}\right)^2 \right]^5}} - 1 \quad (17)$$

has been assigned to the vacuum background, except for the dielectric insulator of the coaxial feeding line. The expedient given by Equation (17) is alternative to perfectly matched layers, whose built-in implementation in the FEM code was not effective for the present geometry. A similar approach is widespread in the simulation of plasma waves in nuclear fusion [35] and profitably applied to EBG structures [36]. For most of next simulations, the values $N_x = 34$ and $N_y = 37$ are enough to achieve a matched dissipative medium that fully absorbs outgoing waves. In a few cases, where lower frequencies are involved, slightly higher values have been used.

The geometries were drawn by creating a rectangular grid of metal and dielectric cylinders in a vacuum background with

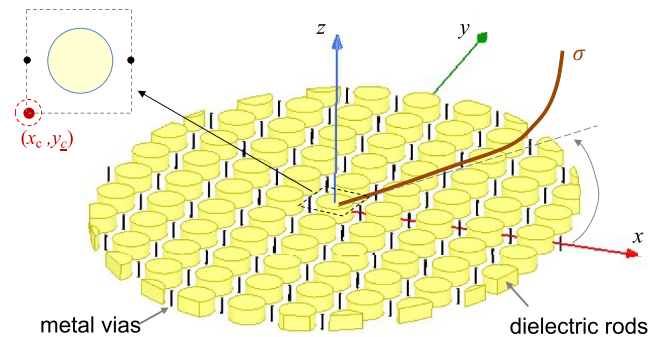


FIGURE 4 Geometry of the finite-element method (FEM) code with $N_x = 4$ and $N_y = 5$. An exemplifying curve of the electrical conductivity is shown too

the electrical conductivity Equation (17), and intersecting all elements with an elliptic cylinder of the aforementioned size, which constitutes the simulation domain. Symmetry planes have been set wherever possible to reduce the computational load by simulating only a sector of the elliptic cylinder in place of the full shape. Without the EBG, a cylindrical wave would be excited in the parallel-plate waveguide, that is, an electromagnetic field that, on the xy plane, presents circular wavefronts with constant amplitude along the azimuthal coordinate. In such a case, a simulation domain with circular cross-section is the best choice. With the EBG, the radiation is focussed along the y axis, which is the propagation direction of the radiation mode. In this case a longer simulation domain along the axis where more energy is focussed is useful because it allows the σ profile to vary more slowly along such direction and to achieve lower reflection and larger absorption of outgoing waves. An elliptic simulation domain, with major axis along y , has been thus adopted to optimise computational efforts: as a term of reference, a typical geometry among the smallest ones has more than 500,000 tetrahedrons.

As far as the modal approach of Section 2 is concerned, the plane-wave expansion method is known to have a low convergence rate in the presence of an abrupt, that is, step-type, periodic variation of the dielectric constant. Figure 5a shows the frequency of the radiation mode as predicted by solving the eigenvalue problem given in the Appendix 1 for an increasing number of harmonics, while in Figure 5b the variation amplitude of such frequency (Δf) between two consecutive computations with different number of harmonics is plotted. The condition $\Delta f < 1$ MHz, which requires at least 10^4 harmonics, was heuristically identified as a satisfactory criterion. Since we are dealing with a two-dimensional Fourier series, this value corresponds to $\sqrt{10^4} = 100$ terms for each summation of Equation (1). To have symmetric summations with an equal number of positive and negative harmonics, in next calculations $(101)^2$ spatial harmonics have been used.

The computation time of a FEM simulation on a workstation with Intel Xeon E5-2643 at 3.4 GHz and 384 GB of RAM is of the order of 20 min for a model with two symmetry planes, that is, for a quarter of the geometry in Figure 4. With

reference to the semi-analytical calculation of R_{in} according to Equation (8), a run with an in-house code on the same workstation takes around 17 min when $(101)^2$ spatial harmonics are taken into account. Less accurate, but still meaningful results can be obtained in a few seconds with a smaller truncation index for the summations in Equations (7) and (10). The computation of Equation (16) is instead immediate given the frequency of the radiation mode.

3.2 | Parametric analyses

This section aims at providing useful guidelines for the design and matching of antennas that exploit the radiation mode. A comprehensive set of analyses is presented to study the dependence of probe impedance on the geometrical and electromagnetic parameters of the lattice as well as to check the reliability of the model of Section 2. The latter relies on two major approximations:

- The current density over the probe has been impressed according to Equation (5). An in-plane variation in the form of Dirac delta function has been assumed, neglecting any effect due to the non-zero diameter of the probe. The variation along z is not self-consistently solved, but enforced as given by Equation (6).
- The radiation mode is only considered, implying that the model is reliable if the lattice is monomodal and the real part of Z_{in} is only concerned.

The second approximation is well verified also in FEM simulations if metal vias are used. At the end of this Section, the case without vias is also considered to show how the monomodal restriction can be worked around for the spurious mode with $k_x = \pi/a$ and $k_y = 0$. Besides the aforementioned approximations, the modal approach presents further differences from a real antenna, some of which have been also neglected in the FEM simulations. The lattice is truncated and, beyond its boundaries, modes encounter free space or metal plates, which cause partial or full reflection respectively. Real

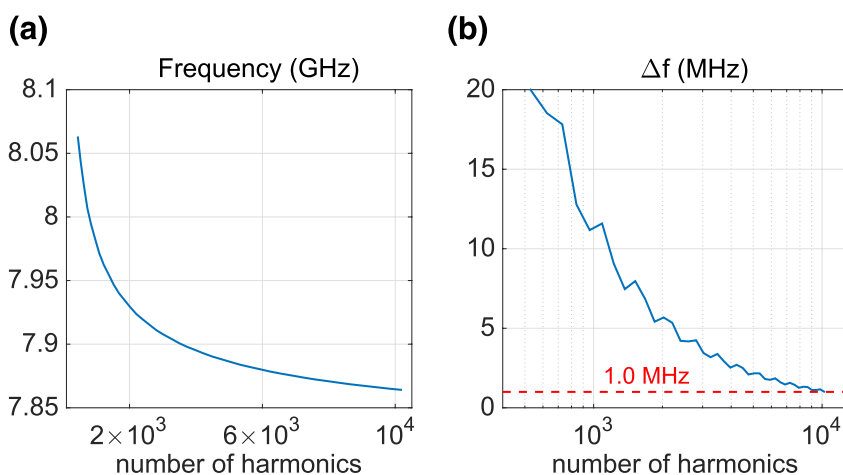


FIGURE 5 Frequency f of the radiation mode (a) in linear scale and Δf (b) in semilog scale versus the number of spatial harmonics used in the computation with the modal approach

materials have losses and in coaxial probes, the dielectric insulator may protrude to some extent out of the cable. As far as probe deviations from a real coaxial connector are concerned, their effect has been assessed with the FEM code. The inner and outer diameters of the feeder have been varied within meaningful ranges of values around the nominal ones, and the filling medium of the coaxial cable has been extended inside the parallel plate waveguide. As a test case, a waveguide height of 1 mm with $b_c = b$, $x_c = -a/2$, $y_c = -a/2$ has been simulated at 7.864 GHz. The point-like approximation of the probe diameter was found to play a negligible role, whereas the change of input resistance due to the variation of probe outer diameter and insulator protrusion was within $\pm 20\%$.

The aforementioned non-idealities prevent the formulation of Section 2 from exactly predicting the value of input impedance for the feeder of a real antenna, but the dependences explored in this section hold true and represent a useful guide in the optimisation of the antenna electrical performance. In next plot legends, the results from the FEM code, the semi-analytical calculation of R_{in} through Equation (8), and the approximate formula (16) will be identified as FEM, numerical, and analytical, respectively.

The variation of probe impedance with respect to the normalised waveguide height h/λ_0 , being λ_0 the vacuum wavelength is plotted in Figure 6. As the height becomes large, the results of the modal approach begin to diverge significantly from the FEM results. This behaviour is due to the first one of the abovementioned approximations, in particular to the current distribution that has been enforced to follow Equation (6). The same behaviour has been already documented with reference to the input impedance of probe-fed microstrip patches [32]. The variation of Z_{in} versus the normalised probe height h_c/h is shown in Figure 7 for a fixed waveguide height of 4.5 mm. It results in an offset between the curves obtained with the FEM and modal approaches; such offset has been also ascribed to the approximation on probe current. The application of either gap feed or magnetic frill models is expected to

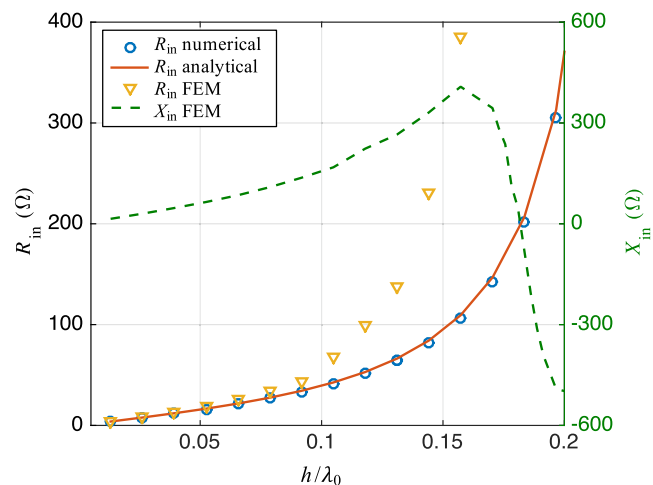


FIGURE 6 Input impedance versus normalised height of parallel-plate waveguide; $a = 10$ mm, $r = 0.35a$, $\epsilon_r = 11.7$, $b_c = b$, $x_c = -a/2$, $y_c = -a/2$, $f = 7.864$ GHz

reduce this offset. It is worth noticing that, before crossing the condition $X_{in} = 0$, the probe reactances of Figures 6 and 7 are inductive and capacitive respectively. In the former case the coaxial probe is indeed short-circuited on the upper waveguide plate ($b_c = b$); in the latter case it terminates with an open circuit ($b_c < b$).

In next analyses, a waveguide height of 1 mm has been considered. For the reference lattice of Figure 3, this value approximately corresponds to $\lambda_d/10$ and $\lambda_0/40$, being λ_d the dielectric wavelength. Figure 8 reports the dependence of input impedance versus the cylinder radius. The plot covers a much larger range of radii than the interval effectively used in antenna design. For $r > 0.4a$, the bandgap vanishes as is clear from Figure 9, explaining a larger disagreement between the FEM code and the modal approach for $r = 0.45a$. The same phenomenon stands out in Figure 10, where the variation of

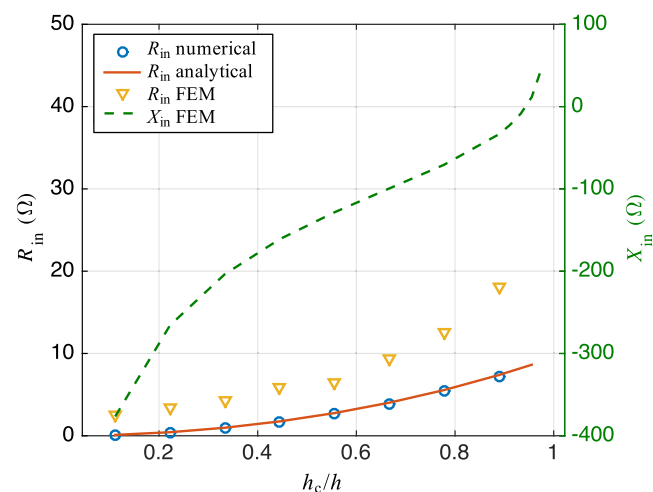


FIGURE 7 Input impedance versus normalised probe height; $a = 10$ mm, $r = 0.35a$, $\epsilon_r = 11.7$, $b = 4.5$ mm, $x_c = -a/2$, $y_c = -a/2$, $f = 7.864$ GHz

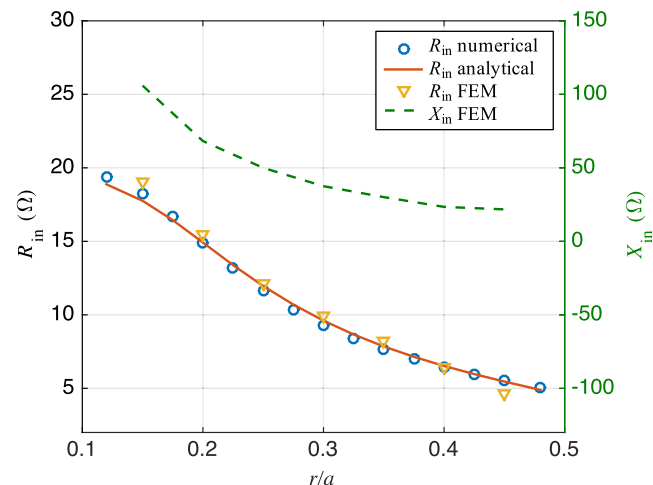


FIGURE 8 Input impedance versus cylinder radius; $a = 10$ mm, $\epsilon_r = 11.7$, $b = b_c = 1$ mm, $x_c = -a/2$, $y_c = -a/2$, f = bottom frequency of the air band, as given by the black line of Fig. 9

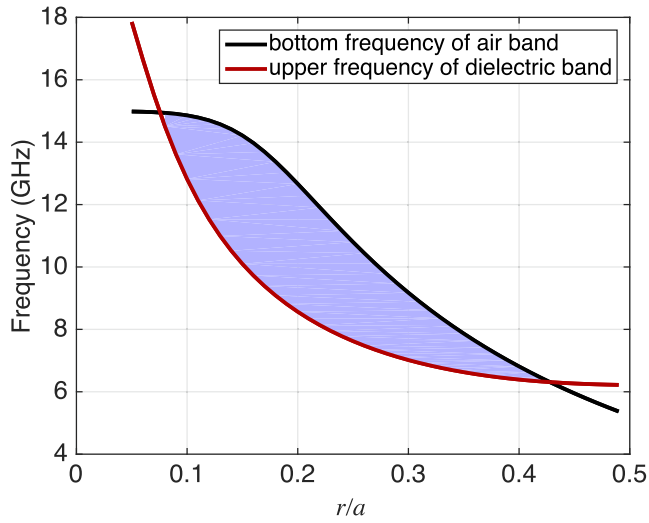


FIGURE 9 Frequency boundaries of the bandgap versus cylinder radius

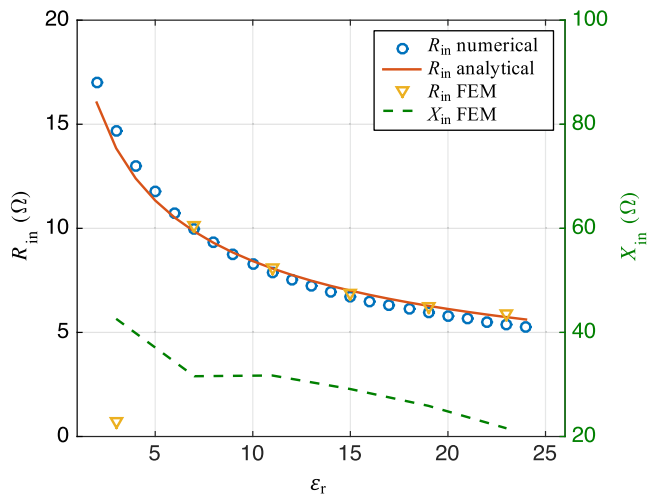


FIGURE 10 Input impedance versus cylinder relative permittivity; $a = 10$ mm, $r = 0.35a$, $b = b_c = 1$ mm, $x_c = -a/2$, $y_c = -a/2$, $f =$ bottom frequency of the air band for the given values of ϵ_r

input impedance versus the cylinder dielectric constant is reported. In this case, the bandgap vanishes for $\epsilon_r < 4$.

Figure 11 shows the variation of input impedance with respect to the probe position along x . Such dependence reflects that of the radiation mode eigenfunction, which is depicted in Figure 18 in the Appendix 1. The variation of Z_{in} versus y_c is not shown because it similarly reflects the eigenfunction value at the same coordinates. In particular, for $x_c = -a/2$ and $y_c = 0$, a nodal line of the eigenfunction is intersected and the radiation mode is not excited, resulting in $R_{in} = 0$ as predicted by Equation (16) too. Similarly, if the degenerate radiation mode were considered, a purely reactive input impedance would be found for $x_c = 0$ and $y_c = \pm a/2$. Namely, with the coaxial probe in such position, there is no need of vias because the radiation mode with $k_x = 0$ and $k_y = \pi/a$ is only excited.

It is now worth considering the situation where both modes are allowed to propagate. Without metal vias, the mode with

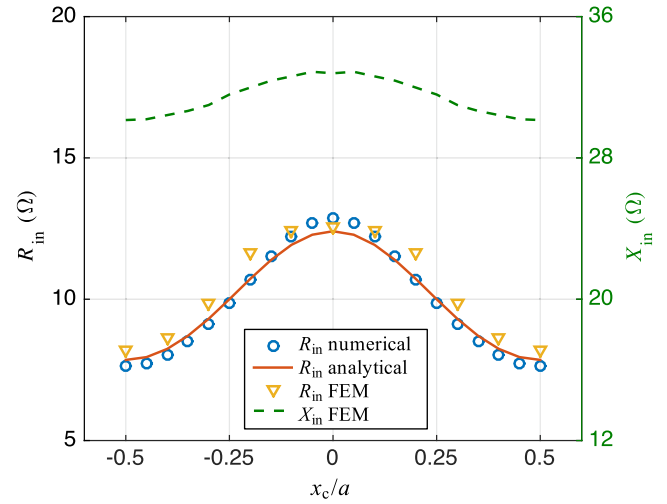


FIGURE 11 Input impedance versus probe position along x ; $a = 10$ mm, $r = 0.35a$, $\epsilon_r = 11.7$, $b = b_c = 1$ mm, $y_c = -a/2$, $f = 7.864$ GHz

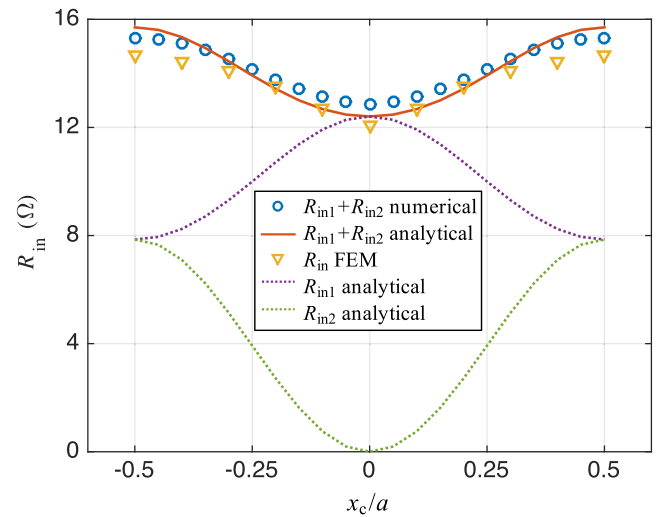


FIGURE 12 Input resistance versus probe position along x in a lattice without vias; $a = 10$ mm, $r = 0.35a$, $\epsilon_r = 11.7$, $b = b_c = 1$ mm, $y_c = -a/2$, $f = 7.864$ GHz. The subscript 1 denotes the mode with $k_x = 0$ and $k_y = \pi/a$; the subscript 2 denotes the mode with $k_x = \pi/a$ and $k_y = 0$

$k_x = \pi/a$ and $k_y = 0$ is also excited as x_c becomes larger or smaller than zero, changing the input impedance. A crude approximation of R_{in} in the absence of vias consists in summing up the input resistances of the two modes. The net effect, which is shown in Figure 12 together with the FEM results is an increasing value of R_{in} as the probe position approaches the corners of the unit cell. The full-wave prediction at $x_c = 0$ is a trifle different from that of Figure 11. This small deviation has been ascribed to the numerical accuracy of the FEM code that in both presence and absence of vias is asked to solve several millions of unknowns.

As far as the probe reactance is concerned, a smooth variation versus lattice parameters can be generally observed in the explored space of parameters. Cylinder radius, cylinder permittivity and probe position determine a relatively weak

dependence of X_{in} , while the probe height exhibits a stronger impact on its value. The probe can be indeed thought as the short- or open-circuited stub of a lossy transmission line. The dependence of the input reactance on the line length is in the form of a hyperbolic tangent or cotangent, while the other lattice parameters mostly affect the primary line constants. This point is further addressed in the next Section.

4 | MATCHING EXAMPLES

4.1 | Infinite lattice

With both open- ($h_c < b$) and short- ($h_c = b$) circuited termination of the coaxial probe, a value of the probe height can be found that satisfies the condition $X_{in} = 0$. By thinking of the probe as a transmission line (TL), it can be intuitively grasped that such condition corresponds to either a resonance or an anti-resonance that alternately recur every half a turn on the Smith Chart. We will refer to such occurrences of $X_{in} = 0$ as TL (anti)resonances and denote the associated probe height with $h_{c, res}^{TL}$. For the unswept lattice parameters of Section 3.2, the value of $h_{c, res}^{TL}$ falls in the neighbourhood of 7 mm, as can be deduced from Figure 6.

Only with the open-circuited probe, the condition $X_{in} = 0$ can be also met with probe heights shorter than 7 mm, as demonstrated by Figure 7. In thin parallel-plate waveguides, the input reactance changes sign as h_c approaches b owing to the capacitive effects resulting from the gap formed by the probe tip and the top plate of the waveguide. Within this regime of reactance cancellation via gap capacitance ($h \lesssim h_{c, res}^{TL}$), the resonant probe height increases with the height of the parallel-plate waveguide. Beyond the TL (anti)resonance, the resonant probe height becomes *quantised*, that is, their values are independent from the height of the parallel-plate waveguide, and their multiplicity is ruled by the turns on the Smith Chart.

The input resistance at resonance, as a function of the parallel-plate waveguide height, reflects the aforementioned behaviour. As illustrated in Figure 13, it increases when the resonant h_c increases, consistently with Figure 7, and slightly decreases while entering the TL resonance regime, because the resonant h_c is becoming constant. The maximum value of the input resistance at the resonance is around 26 Ω , leading to an acceptable matching at the frequency of the radiation mode. According to Figure 11, the input resistance can be increased by moving the coaxial probe from $x_c = -a/2$ to $x_c = 0$. The matching undergoes the enhancement depicted in Figure 14, where the S_{11} at the input of the coaxial feeder is plotted versus frequency.

4.2 | Finite-size lattice

The outcomes of the present work have been applied experimentally to seek enhancements for the high reflection coefficient of an existing antenna [14] without relying on external

matching circuits. The antenna, designed to work at 10 GHz exploiting the radiation mode is described in Figure 15, where the geometrical details of the coaxial feeder are given too. Commercial off-the-shelf coaxial probes are available with fixed values of A and B and those procured from chosen vendor, which are $A = 8$ mm and $B = 15$ mm, are not optimal for this antenna. Full-wave calculations return an input impedance approximately equal to $27 - j120 \Omega$, which entails a high voltage standing wave ratio. The simulations were carried out surrounding the structure with perfectly matched layers and applying de-embedding port operations to express the input impedance in the same reference place of previous Sections. The time-domain electromagnetic solver of a commercial software was used, modifying the standard convergence threshold with a more severe one because the unmatched conditions may produce inaccurate results with the general-purpose solver settings.

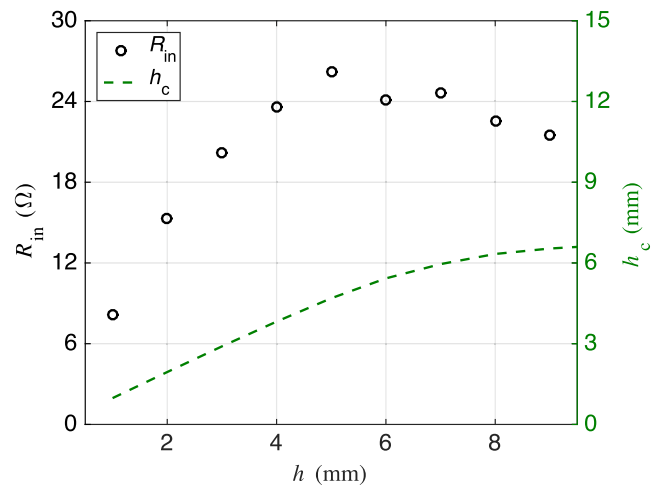


FIGURE 13 Finite-element method (FEM) results of the input resistance and resonant probe height versus waveguide height; $a = 10$ mm, $r = 0.35a$, $\epsilon_r = 11.7$, $x_c = -a/2$, $y_c = -a/2$, $f = 7.864$ GHz

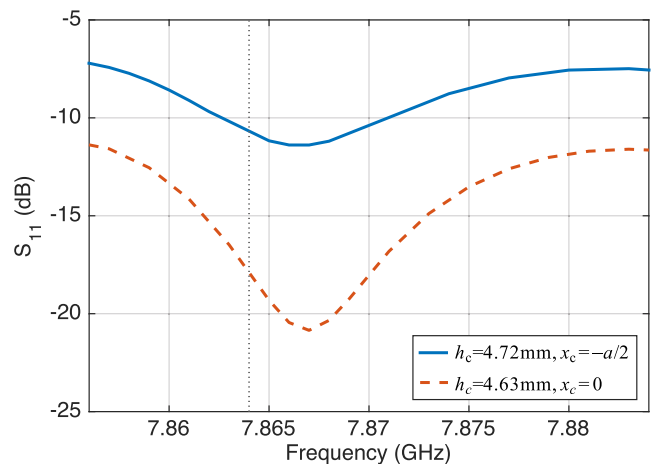


FIGURE 14 Reflection coefficient at the input of the coaxial probe predicted by the finite-element method (FEM) code for $a = 10$ mm, $r = 0.35a$, $\epsilon_r = 11.7$, $b = 5$ mm, $y_c = -a/2$

By varying the height h_c of the probe, the condition $X_{in} = 0$ is readily satisfied with $A = 0$ mm and $B = 8.2$ mm, but the input resistance at the resonance is as low as 13Ω , corresponding to a S_{11} of only -4.8 dB. In this case, a shift of the probe position would make the antenna asymmetric and it would require to manufacture a new bottom plate. Similarly, the other approaches that allow for an increase of the input resistance according to Section 3.2, like changing cylinder radius or permittivity, also affect the radiation performance of

the antenna [37]. All of them require to re-design the lattice and, consequently, to realise a new antenna, except for one approach that can be easily implemented in the current prototype, that is, removing the vias. With this modification, the enhancement of S_{11} is negligible if the original non-optimised coaxial probe of Figure 15 is used, but a good matching is now achieved when probe height is optimised, that is, with $A = B = 8$ mm. A photograph of the antenna and the optimised coaxial feeder is shown in Figure 16. Figure 17,

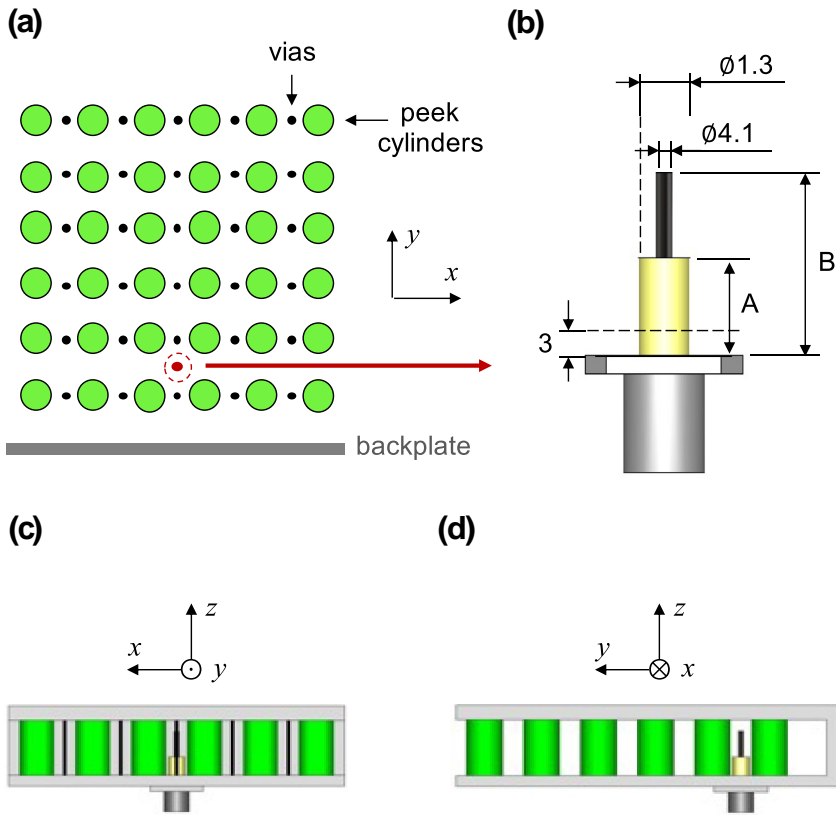


FIGURE 15 Cylinder arrangement (a), coaxial probe (b), front (c), and side (d) views of an antenna exploiting the radiation mode. The antenna is based on a 6×6 lattice of peek ($\epsilon_r = 3.1$, $\tan \delta = 0.01$) cylinders with $a = 13.4$ mm, $r = 4.29$ mm, $h = 15$ mm, interleaved along the rows by stainless steel vias with a radius of 0.4 mm. Aluminium is used for the parallel plates of Fig. 2 and the backplate at the bottom of the lattice. The feeder is a panel-mounted 50- Ω coaxial probe with polytetrafluoroethylene (PTFE) insulator. Dimensions are in mm

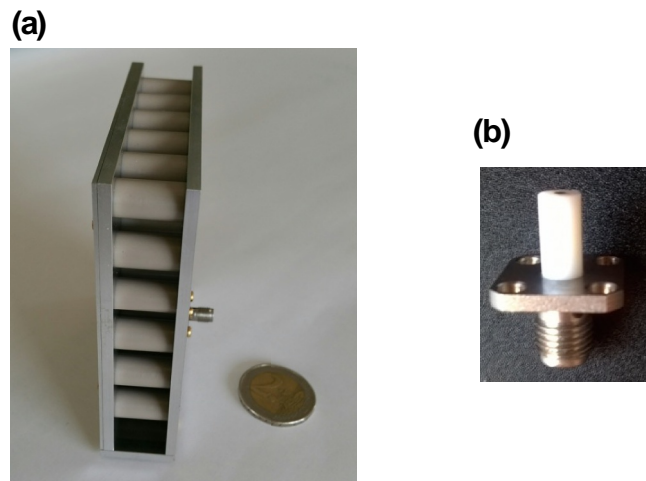


FIGURE 16 Antenna prototype (a) and optimised coaxial feeder (b)

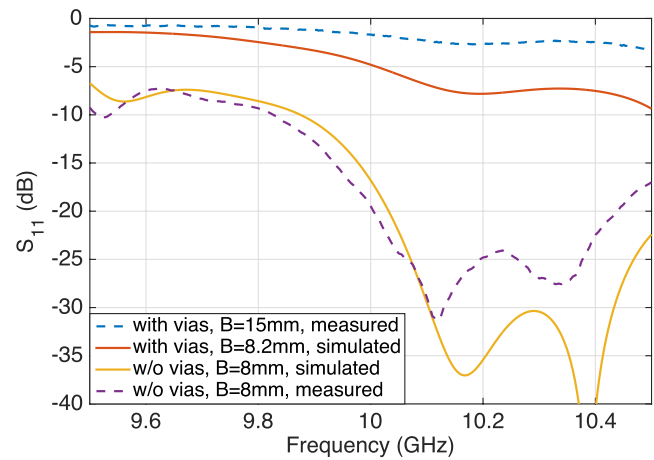
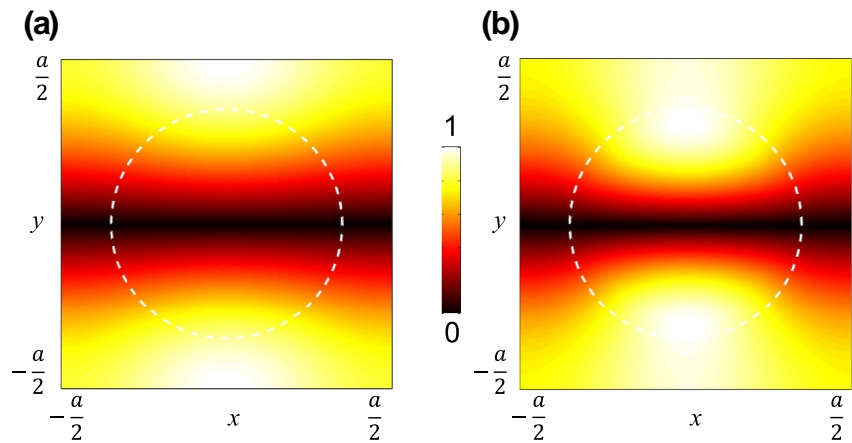


FIGURE 17 S_{11} of antenna configurations with or without vias, fed by original or optimised probes

FIGURE 18 Approximate (a) and rigorous (b) calculations of the normalised $|E_z|$ at the bottom of the air band. The dashed white lines trace the cylinder contour



reporting the simulated and measured S_{11} with the original and modified probes, attests the improvement. The simulations have been carried out with a time-domain full-wave commercial software. The matching has been achieved at the expenses of the radiation performance because the degenerate lattice mode is also excited without vias, entailing a reduction in the directivity and side lobe level of around 2 and 6 dB respectively. This example suggests that an antenna can be probably matched *ex post* without relying on an external network, but a joint optimisation of its electrical and radiation performances should be preferably pursued during the design phase because the lattice parameters affect both the matching and the radiation pattern.

5 | CONCLUSION

The paper has addressed a square lattice of dielectric cylinders, placed in a parallel-plate waveguide and fed with a coaxial probe. This geometry is employed in EBG antennas with an embedded source that excites a lattice mode right above the bandgap. The input resistance of the feeding probe has been studied both numerically and analytically. In particular, an approximate, closed-form expression of the probe resistance has been derived and its validity checked. A thorough analysis of such resistance with respect to the lattice parameters has been performed which unveils the main functional dependences and shows a good agreement between the different approaches when the waveguide height is electrically short. The same parametric study has been numerically carried out for the probe reactance, showing both inductive and capacitive behaviours as a function of the ratio between the probe and the waveguide height.

Numerical results demonstrate that antenna resonances can be achieved by adjusting the probe height and compact (i.e., shorter) resonant antennas can be designed when the probe termination is an open circuit. Input resistances at resonances are usually lower than the standard impedances of coaxial feeders. To attain good matching, they can be increased by using dielectric cylinders with smaller radius, smaller permittivity, longer height or by moving the probe position. The guidelines coming from parametric analyses have been applied to a couple

of examples. Good matching has been achieved in the case of both an infinite lattice and a realistic antenna, suggesting, in the latter case, the need of a combined optimisation of both electrical and radiation parameters during its design. To the best of authors' knowledge, the results of this paper represent the first step of a systematic study for the electrical input parameters of EBG antennas based on lattice modes.

ACKNOWLEDGEMENTS

This work was supported in part by the Italian Ministry for Education, University, and Research under the project PRIN2017 'Quick, reliable, cost effective methodology for Diagnostics of Conformal Antennas (DI-CA),' grant number 20177C3WRM_003.

CONFLICT OF INTEREST

The authors declare no conflict of interest.

DATA AVAILABILITY STATEMENT

The data that support the findings of this study are available from the corresponding author upon reasonable request.

ORCID

Silvio Ceccuzzi  <https://orcid.org/0000-0003-1448-5793>

REFERENCES

- de, P.: Maagt. Photonic bandgap technology. *Commun. Eng.* 1(3), 44–47 (2003)
- Weily, A.R., et al.: Experimental woodpile ebg waveguides, bends and power dividers at microwave frequencies. *Electron. Lett.* 42(1), 32–33 (2006). <https://doi.org/10.1049/el:20063206>
- Pa, P., et al.: Multi-material additive manufacturing of embedded low-profile antennas. *Electron. Lett.* 51(1), 1561–1562 (2015). <https://doi.org/10.1049/el.2015.2186>
- Jun, S., Sanz-Izquierdo, B., Parker, E.A.: 3D printing technique for the development of non-planar electromagnetic bandgap structures for antenna applications. *Electron. Lett.* 52(3), 175–176 (2016). <https://doi.org/10.1049/el.2015.3637>
- Ponti, C., et al.: Tapered all-dielectric EBGs with 3D additive manufacturing for high-gain resonant-cavity antennas. *IEEE Trans. Antenn. Propag.* 69(5), 2473–2480 (2021). <https://doi.org/10.1109/tap.2020.3030924>
- Lu, Y.-F., Lin, Y.-C.: Electromagnetic band-gap based corrugated structures for reducing mutual coupling of compact 60 ghz cavity-backed

- antenna arrays in low temperature co-fired ceramics. *IET Microw. Antennas Propag.* 7(5), 754–759 (2013). <https://doi.org/10.1049/iet-map.2012.0674>
7. Al-Naib, I., Withayachumnankul, W.: Recent progress in terahertz metasurfaces. *J. Infrared, Millim. Terahertz Waves.* 38(9), 1067–1084 (2017). <https://doi.org/10.1007/s10762-017-0381-2>
 8. Enoch, S., et al.: A metamaterial for directive emission. *Phys. Rev. Lett.* 89(21), 213902 (2002). <https://doi.org/10.1103/physrevlett.89.213902>
 9. Pajewski, L., Rinaldi, L., Schettini, G.: Enhancement of directivity using 2D-electromagnetic crystals near the band-gap edge: a full-wave approach. *Prog. Electromagn. Res.* 80, 179–196 (2008). <https://doi.org/10.2528/pterr07111504>
 10. Ceccuzzi, S., et al.: Directive EBG antennas: a comparison between two different radiating mechanisms. *IEEE Trans. Antenn. Propag.* 62(10), 5420–5424 (2014). <https://doi.org/10.1109/tap.2014.2346174>
 11. Yarga, S., Sertel, K., Volakis, J.L.: Degenerate band edge crystals for directive antennas. *IEEE Trans. Antenn. Propag.* 56(1), 119–126 (2008). <https://doi.org/10.1109/tap.2007.912955>
 12. Huang, X., et al.: Dirac cones induced by accidental degeneracy in photonic crystals and zero-refractive-index materials. *Nat. Mater.* 10(8), 582–586 (2011). <https://doi.org/10.1038/nmat3030>
 13. Ceccuzzi, S., et al.: Effect of source position on directive radiation in EBG structures with Epsilon-Near-Zero behavior. *IEEE Antenn. Wireless Propag. Lett.* 18(6), 1253–1257 (2019). <https://doi.org/10.1109/lawp.2019.2913997>
 14. Ceccuzzi, S., Ponti, C., Schettini, G.: Directive EBG antennas based on lattice modes. *IEEE Trans. Antenn. Propag.* 65(4), 1691–1699 (2017). <https://doi.org/10.1109/tap.2017.2670599>
 15. Zeb, B.A., Esselle, K.P.: Design and measurements of a tri-band one-dimensional electromagnetic bandgap resonator antenna. *IET Microw. Antennas Propag.* 10(2), 168–172 (2016). <https://doi.org/10.1049/iet-map.2015.0301>
 16. Enoch, S., Tayeb, G., Maystre, D.: Dispersion diagrams of Bloch modes applied to the design of directive sources. *Prog. Electromagn. Res.* 41, 61–81 (2003). <https://doi.org/10.2528/pterr02010803>
 17. Ceccuzzi, S., Ponti, C., Schettini, G.: Gain enhancement of dipolar antennas employing EBG media. In: 2015 9th International Congress on Advanced Electromagnetic Materials in Microwaves and Optics, pp. 546–548. *METAMATERIALS* (2015)
 18. Eshrah, I.A., Kishk, A.A.: Electric-type dyadic Green's functions for a corrugated rectangular metaguide based on asymptotic boundary conditions. *IEEE Trans. Antenn. Propag.* 55(2), 355–363 (2007). <https://doi.org/10.1109/tap.2006.889913>
 19. Valero-Nogueira, A., et al.: Practical derivation of slot equivalent admittance in periodic waveguides. *IEEE Trans. Antenn. Propag.* 61(4), 2321–2324 (2012)
 20. Valerio, G., et al.: Input impedance of nonperiodic sources exciting 1-D periodic shielded microstrip structures. *IEEE Trans. Microw. Theor. Tech.* 58(7), 1796–1806 (2010). <https://doi.org/10.1109/tmtt.2010.2049919>
 21. Bakhtafrouz, A., Borji, A.: Input impedance and radiation pattern of a resonant dipole embedded in a two-dimensional periodic leaky-wave structure. *IET Microw. Antennas Propag.* 9(14), 1567–1573 (2015). <https://doi.org/10.1049/iet-map.2015.0324>
 22. Harrington, R.F.: Time-harmonic electromagnetic fields. In: *IEEE Press Series on Electromagnetic Wave Theory*. Wiley (2001)
 23. Bhattacharjee, A.K., et al.: Input impedance of rectangular microstrip antennas. *IEEE Proceedings H (Microwaves, Antennas and Propagation)*. 135(1), 351–352 (1988). <https://doi.org/10.1049/ip-h-2.1988.0072>
 24. Pichon, P., Mosig, J., Papiernik, A.: Input impedance of arbitrarily shaped microstrip antennas. *Electron. Lett.* 24(1), 1214–1215 (1988). <https://doi.org/10.1049/el:19880825>
 25. Guha, D., Biswas, M., Siddiqui, J.Y.: Harrington's formula extended to determine accurate feed reactance of probe-fed microstrip patches. *IEEE Antenn. Wireless Propag. Lett.* 6, 33–35 (2007). <https://doi.org/10.1109/lawp.2007.890766>
 26. Carver, K., Mink, J.: Microstrip antenna technology. *IEEE Trans. Antenn. Propag.* 29(1), 2–24 (1981). <https://doi.org/10.1109/tap.1981.1142523>
 27. Abhari, R., Eleftheriades, G.V., van Deventer, T.E.: Equivalent circuit for multiple vias in parallel plate environment. *Electron. Lett.* 36(1), 1446–1447 (2000). <https://doi.org/10.1049/el:20001036>
 28. Zhang, Y., Fan, J.: An intrinsic circuit model for multiple vias in an irregular plate pair through rigorous electromagnetic analysis. *IEEE Trans. Microw. Theor. Tech.* 58(8), 2251–2265 (2010). <https://doi.org/10.1109/tmtt.2010.2052956>
 29. Ueda, T., Lai, A., Itoh, T.: Demonstration of negative refraction in a cutoff parallel-plate waveguide loaded with 2-D square lattice of dielectric resonators. *IEEE Trans. Microw. Theor. Tech.* 55(6), 1280–1287 (2007). <https://doi.org/10.1109/tmtt.2007.897753>
 30. Prather, D.W., et al.: Photonic crystals, theory, applications and fabrication. In: *Wiley Series in Pure and Applied Optics*. Wiley (2009)
 31. Baccarelli, P., et al.: Leaky-wave radiation from 2-D dielectric lattices excited by an embedded electric line source. *IEEE Trans. Antenn. Propag.* 69(11), 7404–7418 (2021). <https://doi.org/10.1109/tap.2021.3083768>
 32. Xu, H., Jackson, D.R., Williams, J.T.: Comparison of models for the impedance of a probe in a parallel plate waveguide and a microstrip patch. In: *IEEE Antennas and Propagation Society International Symposium Digest*, vol. 3, pp. 124–127 (2003)
 33. Pozar, D.M.: *Microwave Engineering*, 4th ed. Wiley (2011)
 34. Collin, R.E.: *Foundations for microwave engineering*. In: *IEEE Press Series on Electromagnetic Wave Theory*. Wiley (2001)
 35. Kaufman, M.: *Lower Hybrid Experiments Using an Interdigital Line Antenna on the Reversed Field Pinch*. PhD thesis, Wisconsin-Madison University, (2009)
 36. Ceccuzzi, S., et al.: On beam shaping of the field radiated by a line source coupled to finite or infinite photonic crystals. *J. Opt. Soc. Am. A* 33(4), 764–770 (2016). <https://doi.org/10.1364/josaa.33.000764>
 37. Ceccuzzi, S., et al.: Radiation shaping by using lattice modes in a dual-feed dielectric structure. In: 2020 14th European Conference on Antennas and Propagation (EuCAP), pp. 1–4 (2020)

How to cite this article: Ceccuzzi, S., et al.: On the input impedance of probe-fed electromagnetic bandgap antennas based on lattice modes. *IET Microw. Antennas Propag.* 16(14), 847–859 (2022). <https://doi.org/10.1049/mia2.12292>

APPENDIX

Compact expression of the electric field

An approximate, compact form of Equation (1) can be derived by retaining very few harmonics of the summation. To this aim, the field is now written as a product of three terms

$$E_z^\pm(x, y) = X(x)Y(y)e^{\mp i(k_x x + k_y y)} \quad (A1)$$

that is, factorised in a phase term and two periodic functions, which only depend on either x or y coordinate. The wave equation can be solved twice considering in turn only harmonics along either x ($n = 0$) or y ($m = 0$) to find simple closed-form expressions of $X(x)$ and $Y(y)$ respectively. In both cases, the wave equation has to be solved for the TM^z modes of the second Brillouin band (air band) with $k_x = 0$ and $k_y = \pi/a$. This equation has the form of the following eigenvalue problem [30]:

$$\sum_m \sum_n |\mathbf{G}_{pq} - \mathbf{k}| \kappa \sqrt{(p-m)^2 + (q-n)^2} |\mathbf{G}_{mn} - \mathbf{k}| \tilde{f}_{mn} = \frac{\omega^2}{c^2} \tilde{f}_{pq}$$

where

$$\mathbf{G}_{mn} = \frac{2\pi m}{a} \hat{\mathbf{x}} + \frac{2\pi n}{a} \hat{\mathbf{y}}$$

$$\tilde{f}_{mn} = |\mathbf{G}_{mn} - \mathbf{k}| f_{mn} \tag{A2}$$

and κ_ℓ are the Fourier coefficients of $1/\kappa(x, y)$, being $\kappa(x, y)$ the periodic function that expresses the spatial variation of the relative permittivity. For a lattice of dielectric cylinder in a vacuum background, $\kappa(x, y)$ is 1 outside them and ϵ_r inside them. The expression of κ_ℓ is given in Equation (13) [30].

As far as $X(x)$ is concerned, a good approximation of the spatial variation of E_z can be achieved with three harmonics (m, n) $(0, -1)$ $(0, 0)$ and $(0, +1)$. The eigenvalue problem can be recast in matrix form

$$\frac{\pi^2}{a^2} \begin{bmatrix} 5\kappa_0 & \sqrt{5}\kappa_1 & 5\kappa_2 \\ \sqrt{5}\kappa_1 & \kappa_0 & \sqrt{5}\kappa_1 \\ 5\kappa_2 & \sqrt{5}\kappa_1 & 5\kappa_0 \end{bmatrix} \cdot \begin{bmatrix} \tilde{f}_{0,-1} \\ \tilde{f}_{0,0} \\ \tilde{f}_{0,+1} \end{bmatrix} = \frac{\omega^2}{c^2} \begin{bmatrix} \tilde{f}_{0,-1} \\ \tilde{f}_{0,0} \\ \tilde{f}_{0,+1} \end{bmatrix} \tag{A3}$$

leading to the following eigenvectors

$$\tilde{f}_{0,-1} = \tilde{f}_{0,+1} = 1$$

$$\tilde{f}_{0,0} = -\frac{4\kappa_0 + 5\kappa_2 + \sqrt{40\kappa_1^2 + (4\kappa_0 + 5\kappa_2)^2}}{2\sqrt{5}\kappa_1} \tag{A4}$$

By using Equations (A4) and (A3) in Equation (1) and doing some mathematical manipulations, we get

$$X(x) = \frac{2a}{\sqrt{5}\pi} \left[\cos\left(\frac{2\pi x}{a}\right) - \frac{5\kappa_0 + 5\kappa_2 - (k_0 a / \pi)^2}{2\kappa_1} \right] \tag{A5}$$

With reference to $Y(y)$, the same procedure is followed, but two harmonics, that is, $(0, -1)$ and $(0, 0)$, are only used, giving

$$Y(y) = \frac{2ja}{\pi} \sin\left(\frac{\pi y}{a}\right) e^{-\frac{j\pi y}{a}} \tag{A6}$$

that represents a good enough approximation for the scopes of this paper.

In Figure 18 the magnitude of the electric field inside a unit cell, normalised to its maximum is shown as obtained by two different calculations. The former uses Equations (A1) with (A5) and (A6), whereas the other relies on Equation (1) with summation indices ranging from -8 to $+8$.